Three-dimensional maps of grain boundaries and the stress state of individual grains in polycrystals and powders

H. Poulsen, S. Nielsen, E. Lauridsen, S. Schmidt, R. Suter, U. Lienert, L. Margulies, T. Lorentzen, D. Juul Jensen

Three-dimensional maps of grain boundaries and the stress state of individual grains in polycrystals and powders

H. F. Poulsen, S. F. Nielsen, E. M. Lauridsen, S. Schmidt, R. M. Suter, U. Lienert, L. Margulies, T. Lorentzen and D. Juul Jensen

ª Materials research Department, Riso National Laboratory, DK-4000 Roskilde, Denmark
ᵇ Department of Physics, Carnegie Mellon University, Pittsburg, PA 15213, USA
ᶜ European Synchrotron Radiation Facilility, BP 220, F-38043 Grenoble Cedex, France

A fast and non-destructive method for generating three-dimensional maps of the grain boundaries in undeformed polycrystals is presented. The method relies on tracking of micro-focused high-energy X-rays. It is verified by comparing an electron microscopy map of the orientations on the 2.5 × 2.5 mm surface of an aluminium polycrystal with tracking data produced at the 3DXRD microscope at the European Synchrotron Radiation Facility. The average difference in grain boundary position between the two techniques is 26 μm, comparable with the spatial resolution of the 3DXRD microscope. As another extension of the tracking concept, algorithms for determining the stress state of the individual grains are derived. As a case study, 3DXRD results are presented for the tensile deformation of a copper specimen. The strain tensor for one embedded grain is determined as a function of load. The accuracy on the strain is $\Delta \epsilon \simeq 10 -4$.

1. Introduction

At Risø we have recently developed several methods for non-destructive characterization of the individual grains inside bulk materials (Poulsen *et al.*, 1997; Lienert, Poulsen, Honki-mäki *et al.*, 1999; Nielsen, Wolf *et al.*, 2000; Juul Jensen, Kvick *et al.*, 2000). The methods are based on diffraction of high-energy X-rays ($E \geq 50$ keV), enabling three-dimensional studies within specimens of millimetre-to-centimetre thickness. In collaboration with the European Synchrotron Radiation Facility (ESRF), the methods have been implemented at the three-dimensional X-ray diffraction (3DXRD) microscope, a dedicated instrument situated at the ID-11 Materials Science Beamline (Lienert *et al.*, 1999). The instrument operates with monochromatic micro-focused beams in the 50–100 keV range. The focal spot sizes are 1 μm × 1 mm and 5 × 5 μm for beams focused in one and two dimensions, respectively.

For undeformed or weakly deformed polycrystals or powders, tracking is the method of choice. Tracking combines the conventional 'rotation method' with ray tracing of the diffracted beams. A program, *GRAINDEX*, has been established that can index the reflections from several hundred grains simultaneously and derive the positions, volumes and orientations of the grains. The data acquisition procedures and software algorithms are both fast, typically requiring of the order a few minutes. Hence, studies of grain dynamics under realistic processing conditions are possible. As such, the first applications of the tracking method relates to *in situ* studies of recrystallization (Lauridsen *et al.*, 2000; Juul Jensen & Poulsen,

2000) and deformation (Margulies *et al.*, 2001) of metals. The details of the tracking principle and the *GRAINDEX* algorithm are presented by Lauridsen *et al.* (2001).

In this article, we extend the tracking concept in two ways. First we establish the geometry and algorithms for a fast and conceptually simple method of mapping the grain boundaries in three dimensions. A combined 3DXRD and electron microscopy study verifies the method, which works for unde-formed and coarse-grained specimens. Next, we discuss two approaches to determine the elastic strain tensors of the grains. One of these is verified by an *in situ* deformation study of a copper polycrystal.

2. Review of the tracking principle

The tracking procedure combines the monochromatic 'rotation method' with X-ray tracing. The principle is sketched in Fig. 1. The incoming beam is focused in one dimension to illuminate a layer in the sample. The divergence of this beam is assumed to be negligible. The sample is mounted on an ω rotation table, with the rotation axis perpendicular to the illuminated plane. For a given ω setting, some of the grains intersected by the layer will give rise to diffracted beams, which are transmitted through the sample to be observed as spots by a flat two-dimensional detector. The detector is aligned perpendicular to the monochromatic beam. In addition, an optional slit can be placed before the sample.

The tracking algorithm works as follows. Images are acquired at a number of rotation-axis-to-detector distances, L_1

to L_N. Equivalent spots, relating to the same reflection, are identified and a best fit to a line through the centre-of-mass (CM) positions of these spots is determined. Extrapolating the line to its intersection with the layer defined by the monochromatic beam, the CM position of the section of the grain, (x_l, y_l), is found, as well as the Bragg angle 2θ and the azimuthal angle η. For definitions of zero points and positive directions of these angles see Fig. 1.

To obtain information from all the grains in one layer, the X-ray tracing is repeated at a number of ω settings in steps of $\Delta\omega$. During each exposure, the sample is oscillated by $\pm\Delta\omega/2$. For high-energy X-rays, an ω range of $180°$ assures that virtually all reflections can be included in the analysis; this justifies the use of a sample stage with only one rotation. However, typically an ω range of $25\text{–}40°$ is sufficient. Finally, for a complete three-dimensional mapping, the procedure is repeated for a set of layers by translating the sample in z.

For each layer, the program *GRAINDEX* sorts the reflections and identifies grains, complete with an orientation matrix **U** and a list of indexed reflections. For the details of the data analysis, see the paper by Lauridsen *et al.* (2001); however, for reference purposes we present the basic equation

$$\mathbf{G}_l = \mathbf{\Omega}\mathbf{S}\mathbf{U}\mathbf{B}\mathbf{G}_{hkl}. \quad (1)$$

Here $\mathbf{G}_l$ is the scattering vector as determined in the laboratory system defined in Fig. 1. $\mathbf{\Omega}$, $\mathbf{S}$ and $\mathbf{U}$ are rotation matrices between the laboratory system (index l), a system rigidly attached to the ω turntable (index ω), a sample system (index s) and a Cartesian coordinate system for a specific grain (index c): $\mathbf{G}_l = \mathbf{\Omega}\mathbf{G}_\omega$, $\mathbf{G}_\omega = \mathbf{S}\mathbf{G}_s$, $\mathbf{G}_s = \mathbf{U}\mathbf{G}_c$. $\mathbf{G}_{hkl}$ is a vector comprising the Miller indices, $\mathbf{G}_{hkl} = (h, k, l)$. The reciprocal-lattice parameters are contained in the **B** matrix

$$\mathbf{B} = \begin{bmatrix} a^* & b^*\cos(\gamma^*) & c^*\cos(\beta^*) \\ 0 & b^*\sin(\gamma^*) & -c^*\sin(\beta^*)\cos(\alpha) \\ 0 & 0 & c^*\sin(\beta^*)\sin(\alpha) \end{bmatrix} \quad (2)$$

with

$$\cos(\alpha) = \frac{\cos(\beta^*)\cos(\gamma^*) - \cos(\alpha^*)}{\sin(\alpha^*)\sin(\beta^*)}. \quad (3)$$

Here $(a, b, c, \alpha, \beta, \gamma)$ and $(a^*, b^*, c^*, \alpha^*, \beta^*, \gamma^*)$ symbolize the lattice parameters in direct and reciprocal space, respectively.

3. Mapping of the grain-boundary topology

For a 'perfect' grain with no orientation spread and an ideal instrument there will be a one-to-one correspondence between the shape of the illuminated cross section of a grain and the shape cross section of any associated diffraction spot. Hence, the position of the grain boundary can be determined by back-projecting the periphery of the diffraction spot along the line established by the X-ray tracing. Introducing a local coordinate system (y_{det}, z_{det}) around the CM of the spot and analogously a system $(\Delta x, \Delta y)$ around the CM of the grain section, the projection becomes

$$y_{det} = \Delta y, \quad z_{det} = \Delta x \tan(2\theta)\cos(\eta). \quad (4)$$

For high-energy X-rays with small Bragg angles, the projection is seen to be very anisotropic. Typically, a square grain section is projected into a rectangular diffraction spot with an aspect ratio of 10:1. Furthermore, for $\eta = 90°$ and $\eta = 270°$, the projection collapses into a line. Hence, diffraction spots appearing within a certain η range around these limits cannot be part of the analysis.

In metallurgy and ceramics research, the grains are seldom truly perfect. Moreover, the instrumental resolution is an issue. Hence, the intensity distribution of a spot on the detector, $I_{det}(y_{det}, z_{det})$, can be seen as the idealized response of a 'perfect' grain, I_0, convoluted with the instrumental resolution function, Res, and the orientation spread of the reflection, Q. Res can be determined with a high degree of accuracy; its main components are the detector response function and the smearing caused by the oscillation in ω during acquisition. In contrast, Q varies from reflection to reflection and is *a priori* unknown. (However, provided that the detector is sufficiently close to the sample, there is no noticeable spread in 2θ.)

The existence of an orientation spread within each grain also implies that some of the reflections will be associated with several diffraction spots appearing in images acquired at neighbouring ω settings. As the ω axis is a fixed point for the rotation, this effect is pronounced for reflections appearing near the axis, *i.e.* for spots with $\eta \simeq 0$ and $\eta \simeq 180°$.

To handle these complications, it seems relevant to use space-filling algorithms based on either intensity conservation constraints or fits to the local orientation function (Monte Carlo simulations). The establishment

Figure 1
Sketch of the tracking principle. The diffraction spots appearing in exposures of the area detector at different sample–detector distances are projected back to the illuminated plane in the sample. The angles $(2\theta, \eta, \omega)$ are defined as well as the laboratory coordinate system.

of such algorithms is outside the scope of this article. Instead, we pursue the simple approach of determining the outlines of the diffraction spots and we back-project the outlines into the sample plane. This approach can be seen as a fast procedure for obtaining a coarse map, to be refined later in the analysis by more advanced algorithms.

We have tested two approaches. In the first, the outline of a given spot was determined by an intensity threshold, fixed at a certain percentage of the maximum pixel intensity within the spot. In the second, the outline was defined by the points of steepest descent. The image-processing program *Image Pro* used by *GRAINDEX* provides routines to find the outline of any object by either method. It is found that the steepest-descent method is more robust. Consequently, this has been used for the data presented here. The problem of a reflection breaking up into several spots is solved by merging the back-projected outlines of the individual parts.

For a given reflection, the back-projected outline can be associated with two types of error. The first is related to the uncertainty in the CM projection. The second reflects the anisotropy in the projection; *cf.* equation (4). Based on these errors, the resulting grain boundary can be determined from a fit to the back-projected outlines of all the reflections associated with the grain. Alternatively, the grain boundary is determined as the back-projected outline of the reflection which has superior projection properties. That is, the one associated with a minimum orientation spread and with the most favourable angular setting, *i.e.* the largest projection factor $\tan(2\theta)\cos(\eta)$ [*cf.* equation (4)].

4. Verification and discussion of the grain mapping principle

To verify the principle, a combined synchrotron and electron microscopy study was performed on a coarse-grained 99.996%-pure aluminium polycrystal. Initially the grains at one surface of the sample were mapped by the electron back-scattered pattern (EBSP) method. In this way, the local orientations on the surface were sampled in a 20×20 μm grid. Some 50 grains were identified.

Next, the sample was aligned with the same surface parallel to the beam at the 3DXRD microscope. The tracking was performed with a line-focused beam of dimensions $800 \times$

5 μm. The beam was parallel to the surface and incident at a layer 10 μm below it. The X-ray energy was $E = 50$ keV and the bandwidth was $\Delta E/E = 0.5\%$. The two-dimensional detector is equipped with a powder scintillator screen, which is coupled by focusing optics (lenses) to a charge-coupled device (CCD). The resulting pixel size is 4.3 μm, but the point-spread function is substantially larger, with a full width at half-maximum (FWHM) of 16 μm.

The range of orientation variations within the grains was found on average to be of the order of $1°$. The surface dimensions of the sample were 2.5×2.5 mm, making it necessary to acquire information from three strips across the sample. For each strip, the tracking procedure was performed with 22 equidistant ω settings with $\Delta\omega = 2°$ and with detector distances $L_1 = 7.6$, $L_2 = 10.3$ and $L_3 = 12.9$ mm. With a 1 s exposure time, the total data acquisition time was less than 4 min.

An example of a set of images acquired at L_1, L_2 and L_3 is given in Fig. 2. The diffraction spots are seen to move outwards from the centre of the images when the detector is translated away from the sample. The error on the linear fit to the CM of such corresponding spots does on average correspond to an uncertainty of ±17 μm along the beam direction in the sample plane.

Fig. 3 is an example of a reflection, where the diffracted intensity is divided into four spots. This kind of break-up into a few large flakes is found to be typical of the specimen. The tracking algorithm associated the four diffraction spots with directions that differed by less than $2°$. Hence, the corresponding four outlines were merged into one, defined as the circumference of the total area enclosed by any of the four outlines. Analogously, diffraction spots associated with the same reflection but appearing in different strips were identified by their common direction, and the outlines once again were merged by superposition.

The outlines of three reflections associated with the same grain are compared in Fig. 4. The direction of the incident beam is in all cases within a few degrees parallel to the vertical direction in the images. The corresponding larger uncertainty on the outlines in this direction is evident. Furthermore, we observe that the reflection with the most favourable angular settings (largest 2θ and η furthest away from the equatorial plane) gives rise to the best correspondence with the EBSP
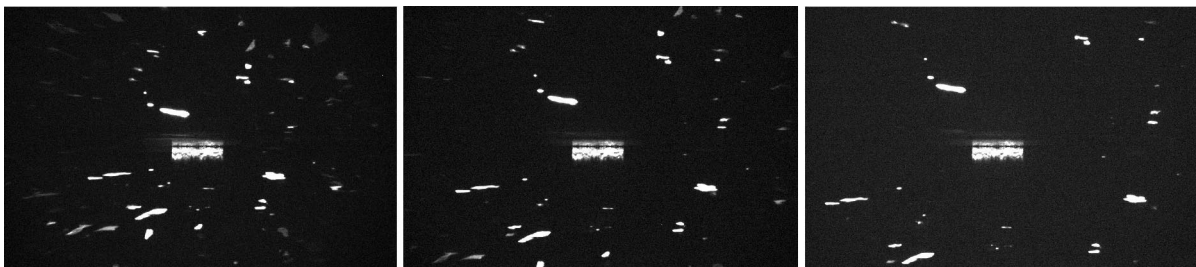
Figure 2
Diffraction patterns from the aluminium polycrystal at sample–detector distances of 7.6 mm (left), 10.3 mm (middle) and 12.9 mm (right). The rectangular spots near the centre of the images are artefacts caused by the tails of the incident beam. The horizontal length of the rectangular spots is 0.8 mm.
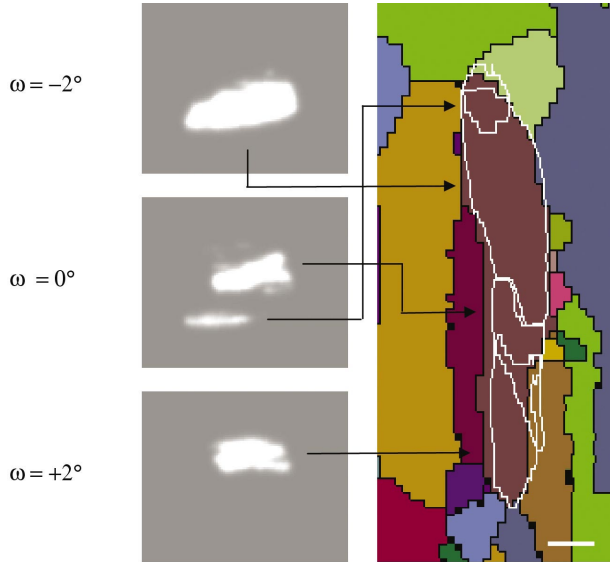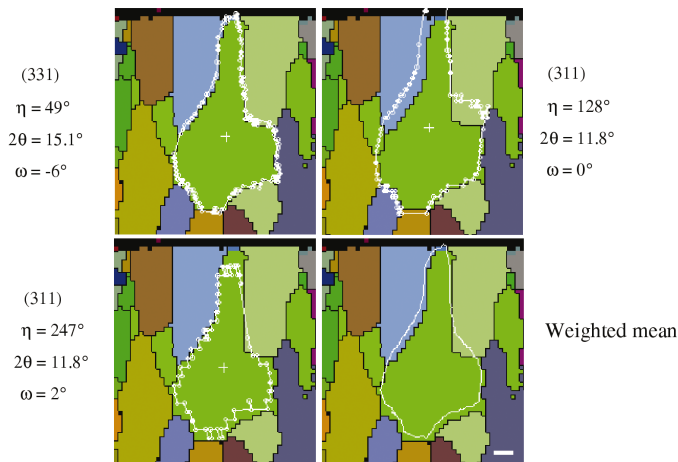
Figure 3
Example of the effect of grain break-up. For this particular reflection, the diffracted intensity is distributed over three images, acquired at $\omega = -2, 0$ and $2°$. Left: identical sections of the images acquired at the three ω settings. Right: the back-projection of the outlines of the four spots into the sample plane (white lines). These are superimposed on an EBSP image of the same section of the sample surface (colours and black lines). The white scale bar at the bottom is 100 μm.

data. Also shown in Fig. 4 is the weighted average of the three outlines. For reasons of robustness and simplicity, we choose to consider only the best reflection in the following.

The grain orientations determined by the tracking routine and by EBSP agreed within $1°$. For comparison, the tracking procedure produced grain orientations with an accuracy of better than $\pm 0.1°$, as determined by the scatter between reflections from the same grain. The difference between the

techniques is therefore thought mainly to arise from EBSP and alignment errors.

In Fig. 5, the resulting EBSP and 3DXRD grain boundaries are superposed. As mentioned, the 3DXRD boundaries are based on data with no interpolation or averaging between reflections from the same or neighbouring grains. The misfit between the tracking and the EBSP boundaries was found by linear intercept to be 26 μm on average with a maximum of 40 μm. These data should be compared with the 16 μm point-spread function of the detector, the 20 μm step size in the EBSP data, and also the 10 μm difference in z.

The degree of correspondence obtained with the crude outline algorithm illustrates the potential of mapping grains in three dimensions. In fact, the quality of the map is sufficient for many basic studies. A first application of such a mapping, namely a study of the wetting of aluminium grain boundaries by liquid gallium, has been published elsewhere (Nielsen, Ludwig *et al.*, 2000). The use of difference maps should also enable grain-boundary mobility studies. More generally, simplified descriptions of the grain morphology in terms of centroids (centre-of-mass position, volume and aspect ratio) can be very useful, especially for classifying grains. Furthermore, it should be recalled that many annealed polycrystals exhibit orientation spreads substantially smaller than $1°$.

Ultimately, for near-perfect grains the limit on the mapping accuracy is governed by the width of the focal line, the detector resolution and the accuracy of the sample movements. With present technology these factors can all be reduced to 1 μm. Indeed, for synchrotron-based X-ray tomography, which is also based on a projection of high-energy X-rays on two-dimensional detectors, a spatial accuracy below 1 μm has been reached (Baruchel *et al.*, 2000).

For grains with an orientation spread above $1°$, the outline formalism breaks down. Two routes can then be followed. The first is to restrict the incoming beam in both directions, such that only a line through the specimen is illuminated. In this

Figure 4
The outline of one grain as determined from three different reflections (white lines). These are superimposed on an EBSP image of the same section of the sample surface (colours and black lines). The image in the lower right corner is a weighted fit to the grain boundary based on the three outlines and estimates of their errors. The white scale bar in the right corner is 100 μm.

Figure 5
Validation of the X-ray tracing algorithm. Colours and black outlines mark the grains and grain boundaries on the surface of the aluminium polycrystal as determined by electron microscopy (EBSP). Superposed as white lines are the grain boundaries resulting from the synchrotron experiment. The scale bar at the bottom is 400 μm.

case, the fact that the orientation spread does not have a radial (2θ) component implies that the one-to-one correspondence can be regained. However, the mapping becomes much slower, as the sample needs to be scanned in both y and z. As an alternative, a conical slit can be inserted between the sample and the detector for a full three-dimensional definition of the gauge volume, at the cost of further reduced data acquisition speed. First mappings with the conical slit were presented by Poulsen *et al.* (1997) and Nielsen, Wolf *et al.* (2000). The second route is to ray-trace the individual parts of the diffraction spot by means of Monte Carlo simulations. Work along both routes as well as work on space-filling routines in general is in progress.

5. Strain formalism

For strain analysis, it is suggested to extend the tracking algorithm by including data at a large sample–detector distance, L_N. The larger distance facilitates a superior 2θ resolution. In practice, two detectors may be used: a moveable and semitransparent one with a small pixel size at short sample–detector distances, and a fixed detector with a larger field of view placed at a large distance.

The elastic strain is a property of the unit cell in each grain. Hence, for each grain we define a Cartesian system with axes $(\mathbf{x}_d, \mathbf{y}_d, \mathbf{z}_d)$ and with $\mathbf{x}_d$ parallel to $\mathbf{a}$, $\mathbf{y}_d$ in the plane of $\mathbf{a}$ and $\mathbf{b}$, and $\mathbf{z}_d$ perpendicular to that plane. In analogy with equation (2), the transformation between the two systems is given by the matrix

$$\mathbf{A} = \begin{bmatrix} a & b\cos(\gamma) & c\cos(\beta) \\ 0 & b\sin(\gamma) & -c\sin(\beta)\cos(\alpha^*) \\ 0 & 0 & c\sin(\beta)\sin(\alpha^*) \end{bmatrix}. \qquad (5)$$

Let $\mathbf{A}_0$ refer to the lattice of a reference grain, typically representing an unstrained situation. Let $\mathbf{A}$ refer to the lattice of the same grain in a strained situation. We then define the matrix $\mathbf{T}$ by

$$\mathbf{T} = \mathbf{A}\mathbf{A}_0^{-1}. \qquad (6)$$

By definition, the strain tensor is

$$\varepsilon_{ij} = \tfrac{1}{2}(\mathbf{T}_{ij} + \mathbf{T}_{ji}) - \mathbf{I}_{ij}, \qquad (7)$$

where $\mathbf{I}$ is the identity matrix.

We identify two approaches to the strain analysis. In the first, the tensor elements are derived from a linear fit to the 2θ shifts. In the second, a full refinement of the unit-cell parameters is performed, based on the combined shift in ω, η and 2θ. We outline a formalism for both methods.

The analysis of the 2θ shift of the reflections is similar to the one used for macroscopic stress and strain determination with neutron diffraction (Allen *et al.*, 1985), with the exception that the sample reference system is replaced by the grain system. For each reflection i, we determine the components (l, m, n) of the unit vector $\mathbf{G}_c/|\mathbf{G}_c|$. For hard X-rays, with small Bragg angles, to a very good approximation there is a linear relation between the shift in 2θ and the strain ε_i:

$$\begin{aligned} \varepsilon_i &= (d_i - d_0)/d_0 \\ &= [\sin(\theta_i) - \sin(\theta_0)]/\sin(\theta_0) \\ &= \begin{pmatrix} l_i & m_i & n_i \end{pmatrix} \begin{pmatrix} \varepsilon_{11} & \varepsilon_{12} & \varepsilon_{13} \\ \varepsilon_{12} & \varepsilon_{22} & \varepsilon_{23} \\ \varepsilon_{13} & \varepsilon_{23} & \varepsilon_{33} \end{pmatrix} \begin{pmatrix} l_i \\ m_i \\ n_i \end{pmatrix}. \qquad (8) \end{aligned}$$

This equation can be solved by the singular-value decomposition procedure for over-determined linear systems. In addition to being simple, this approach is robust towards the grain rotations associated with plastic deformation. The only error sources are therefore the experimental accuracy in 2θ and the provision of a strain-free reference material.

The experimental setup may be simplified by using only one detector and one detector setting L_N. This requires that the grain positions are found in another way, *e.g.* by placing a slit in the incoming beam and monitoring the intensity of reflections while translating the sample with respect to the slit. Small deviations from the assumed position with respect to the rotation axis may also be included as fit parameters. As an example, consider an *in situ* deformation experiment. Assume that the reference values $(2\theta)_0$ for a given grain are defined by the CM of the diffraction spots for the non-deformed sample, determined with the grain centred exactly on the rotation axis. Assume further that in the deformed state, the same grain is offset by $(\Delta x, \Delta y)$ with respect to the axis in the ω system, with Δx and Δy parallel to $\mathbf{x}_\omega$ and $\mathbf{y}_\omega$, respectively. Then

$$\begin{aligned} \varepsilon_i = \begin{pmatrix} l_i & m_i & n_i \end{pmatrix} &\begin{pmatrix} \varepsilon_{11} & \varepsilon_{12} & \varepsilon_{13} \\ \varepsilon_{12} & \varepsilon_{22} & \varepsilon_{23} \\ \varepsilon_{13} & \varepsilon_{23} & \varepsilon_{33} \end{pmatrix} \begin{pmatrix} l_i \\ m_i \\ n_i \end{pmatrix} \\ &- [\cos(\omega_i) + \sin(\omega_i)\sin(\eta_i)/\tan(\theta_i)](\Delta x/L_N) \\ &- [\sin(\omega_i) + \cos(\omega_i)\sin(\eta_i)/\tan(\theta_i)](\Delta y/L_N). \qquad (9) \end{aligned}$$

The ω range covered should be large. Otherwise, only a subset of the elements in the strain tensor will be determined by equation (8) and the triangulation in equation (9) will be associated with a large uncertainty in one of the two positional parameters.

The second approach, using the full angular information, is potentially more powerful, but also more complex. We will only sketch a solution, with some similarities to the algorithm suggested by Chung & Ice (1999) for white-beam characterization. First we note that the plastic deformation of a grain will be accompanied by a rotation. The suggestion is therefore to fit the matrices $\mathbf{U}$ and $\mathbf{B}$ simultaneously, using equation (1). These can be parameterized by the three Euler angles and the reciprocal-lattice parameters, respectively. Next, the direct lattice constants are derived from the reciprocal ones and inserted into $\mathbf{A}$. From equations (6) and (7), this leads to the strain tensor.

The nine-parameter fit is bound to be non-trivial. In particular, the observations are asymmetric with large errors on ω. Likewise, during deformation, the diffraction spots will spread out substantially along η, making the CM derivation prone to error. Furthermore, the spatial distortions in the detector may render the derivation of an absolute metric impossible. Hence,
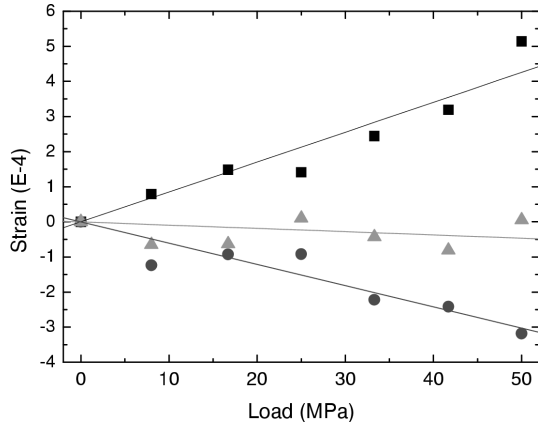
Figure 6
Evolution of selected strain components for an embedded copper grain during tensile deformation. ε_{22} (squares) and ε_{33} (circles) represent directions along the tensile axis and transverse to it, respectively. ε_{23} (triangles) is the associated shear component. Lines represent linear fits to the data.

to facilitate difference measurements, $\mathbf{A}_0$ should be a measured quantity. The advantage of this approach is the complementarity of the 2θ and η variations.

In both cases, the stress tensor σ_{ij} can be derived from the strain tensor by Hooke's law:

$$\sigma_{ij} = \sum_{kl} \mathbf{C}_{ijkl} \varepsilon_{kl}, \qquad (10)$$

where $\mathbf{C}_{ijkl}$ is the compliance tensor, containing the elastic constants.

6. Example of strain-tensor characterization

We report on the first experiment involving strain characterization of single grains as a function of tensile deformation. The experiment was performed at the 3DXRD microscope using an 80 keV X-ray beam focused to a line of 5 μm height. One fixed two-dimensional detector (a Frelon CCD coupled to an image intensifier) was placed 520 mm behind the sample. An undeformed copper specimen with dimensions 3 × 8 × 50 mm was mounted in a 25 kN stress rig. The average grain size was 200 μm. One grain in the middle of the sample was singled out. After each loading step, this grain was centred over the rotation axis and the tracking algorithm performed for an ω range of −30 to 30° and $\Delta\omega = 2°$. The exposure time was 1 s. *GRAINDEX* indexed 21 reflections for this grain, of which four were associated with background problems. Using equation (8), the strain determination was based on the remaining 17 reflections. The result is shown in Fig. 6. Generally, the accuracy $\Delta\varepsilon$ on the strain measurements is

given by the stability of the setup. For the present setup, $\Delta\varepsilon \simeq 10^{-4}$, consistent with the scatter in Fig. 6.

7. Conclusions

We have derived and verified unique methods for mapping the grain boundaries in a polycrystal as well as studying the evolution in the elastic strain in the embedded grains. With the added possibility of grain orientation mapping, the tracking concept is seen to provide a complete structural description on the grain level. The algorithms presented are universal and sufficiently fast (in terms of both hardware and software) that on-line analysis during many types of *in situ* processing studies is feasible.

References

Allen, A., Hutchings, M. T. & Windsor, C. G. (1985). *Adv. Phys.* **34**, 445–473.

Baruchel, J., Cloetens, P., Härtwig, J., Ludwig, W., Mancini, L., Pernot, P. & Schlenker, M. (2000). *J. Synchrotron Rad.* **7**, 196–201.

Chung, J.-S. & Ice, G. E. (1999). *J. Appl. Phys.* **86**, 5249–5255.

Juul Jensen, D., Kvick, Å., Lauridsen, E. M., Lienert, U., Margulies, L., Nielsen, S. F. & Poulsen, H. F. (2000). *Mater. Res. Soc. Symp. Proc.* **590**, 227–240.

Juul Jensen, D. & Poulsen, H. F. (2000). *Proceedings of the 21st Risø International Symposium on Materials Science*, Roskilde, Denmark, pp. 103–124.

Lauridsen, E. M., Juul Jensen, D., Poulsen, H. F. & Lienert U. (2000). *Scr. Mater.* **43**, 561–566.

Lauridsen, E. M., Schmidt, S., Suter, R. M. & Poulsen, H. F. (2001). *J. Appl. Cryst.* **34**, 744–750.

Lienert, U., Poulsen, H. F., Honkimäki, V., Schulze, C. & Hignete, O. (1999). *J. Synchrotron Rad.* **6**, 979–984.

Lienert, U., Poulsen, H. F. & Kvick, Å. (1999). *Proceedings of the 40th Conference of AIAA on Structures, Structural Dynamics and Materials*, St Louis, USA, pp. 2067–2075.

Margulies, L., Winther, G. & Poulsen, H. F. (2001). *Science*, **291**, 2392–2394.

Nielsen, S. F., Ludwig, W., Bellet, D., Lauridsen, E. M., Poulsen, H. F. & Juul Jensen, D. (2000). *Proceedings of the 21st Risø International Symposium on Materials Science*, Roskilde, Denmark, pp. 473–478.

Nielsen, S. F., Wolf, A., Poulsen, H. F., Ohler, M., Lienert, U. & Owen, R. A. (2000). *J. Synchrotron Rad.* **7**, 103–109.

Poulsen, H. F., Garbe, S., Lorentzen, T., Juul Jensen, D., Poulsen, F. W., Andersen, N. H., Frello, T., Feidenhans'l, R. & Graafsma, H. (1997). *J. Synchrotron Rad.* **4**, 147–154.